tvst

Article

Scattering Angle Resolved Optical Coherence Tomography Detects Early Changes in 3xTg Alzheimer's Disease Mouse Model

Michael R. Gardner[1,3], Vikram Baruah[1], Gracie Vargas[2], Massoud Motamedi[2], Thomas E. Milner[1], and Henry G. Rylander, III[1]

[1] Department of Biomedical Engineering, The University of Texas at Austin, Austin, TX, USA
[2] Center for Biomedical Engineering, The University of Texas Medical Branch, Galveston, TX, USA
[3] Department of Biomedical Engineering, King Faisal University, Al-Hofuf, Al-Ahsa, Saudi Arabia

Correspondence: Michael R. Gardner, Department of Biomedical Engineering, King Faisal University, Al-Hofuf, Al-Ahsa, Saudi Arabia.
e-mail: mgardner@kfu.edu.sa

Received: July 22, 2019
Accepted: March 2, 2020
Published: April 24, 2020

Keywords: optical coherence tomography; Alzheimer's disease; neurodegeneration; light scattering; mouse model

Citation: Gardner MR, Baruah V, Vargas G, Motamedi M, Milner TE, Rylander HG III. Scattering angle resolved optical coherence tomography detects early changes in 3xTg Alzheimer's disease mouse model. Trans Vis Sci Tech. 2020;9(5):18, https://doi.org/10.1167/tvst.9.5.18

Purpose: Clinical intensity-based optical coherence tomographic retinal imaging is unable to resolve some of the earliest changes to Alzheimer's disease (AD) neurons. The aim of this pilot study was to demonstrate that scattering-angle-resolved optical coherence tomography (SAR-OCT), which is sensitive to changes in light scattering angle, is a candidate retinal imaging modality for early AD detection. SAR-OCT signal data may be sensitive to changes in intracellular constituent morphology that are not detectable with conventional OCT.

Methods: In this cross-sectional study, retinas of a triple transgenic mouse model of AD (3xTg-AD) were imaged alongside age-matched control mice (C57BL/6J) using SAR-OCT. A total of 32 mice (12 control, 20 3xTg-Ad) at four ages (10, 20, 30, and 45 weeks) were included in this cross-sectional study, and three retinal feature sets (scattering, thickness, and angiography) were examined between the disease and control groups.

Results: AD mice had significantly increased scattering diversity (lower SAR-OCT C parameter) at the earliest imaging time (10 weeks). Differences in the C parameter between AD and control mice were diminished at later times when both groups showed increased scattering diversity. AD mice have reduced retinal thickness compared to controls, particularly in central regions and superficial layers. No differences in vascular density or fractional blood volume between groups were detected.

Conclusions: SAR-OCT is sensitive to scattering angle changes in a 3xTg-AD mouse model and could provide early-stage biomarkers for neurodegenerative diseases such as AD.

Translational Relevance: Clinical OCT systems may be modified to record SAR-OCT images for non-invasive retinal diagnostic imaging of patients with neurodegenerative diseases such as AD.

Introduction

Alzheimer's disease (AD) is the most common of all neurodegenerative diseases. In 2016, about 5.4 million Americans were diagnosed with AD, and of these 5.2 million were 65 years or older.[1] Of Americans 65 years and older, 11% have AD, and 32% of Americans 85 years or older have AD.[2] These numbers are expected to increase as the Baby Boomer generation continues to age and treatment options for other diseases extend lives.[3]

Recent guidelines and criteria for diagnosing AD include a category for a symptomatic, pre-dementia phase termed "mild cognitive impairment due to AD"[4,5]; however, even in this early disease state, significant pathophysiological changes are observed.[6] In fact, changes in the brain can begin more than 20 years prior to the onset of AD symptoms.[7–9] Early detection of AD is believed to represent the best path forward for

efficacious treatment of the disease,[10,11] and delays in AD onset and progression would significantly reduce the global burden of the disease.[12] Early detection methods offer possibilities for initiating early treatment plans and enable monitoring of therapeutic interventions.

Classical histopathological signs of AD include amyloid beta (Aβ) plaques, tau protein tangles, neurofibrillary tangles, and neuronal atrophy,[13] but it is now known that these markers are preceded by functional neurological changes, including synaptic failure.[14] Synaptic failure is associated with mitochondrial dysfunction and altered signaling pathways.[15,16] In healthy neurons, mitochondria maintain a balance between fission and fusion states, dividing and fusing to form robust and vital energy-producing organelle networks. Before classic histologic changes associated with neurodegenerative diseases are initiated, the fission–fusion balance in mitochondria is upset, with the fission state becoming more dominant.[17] Eventually, mitochondrial dysfunction progresses and neurodegenerative disease can be detected by contemporary detection methods.[18] At this stage, available therapeutic interventions are unlikely to significantly delay or reverse the disease, and patients will continue to suffer from cognitive decline.[19]

Furthermore, Aβ is known to trigger neuronal cell loss via the apoptotic pathway.[20,21] In particular, Aβ targets neuronal mitochondria and promotes mitochondrial fission, disruption of mitochondrial membrane potential, increase in intracellular reactive oxygen species levels, and mitophagy activation.[22] Subsequent mitochondrial swelling, mitochondrial channel opening, and rupture can cause the release of cytochrome *c*, which can lead to cellular necrosis or apoptosis.[22–24]

In vivo detection of dysfunctional retinal mitochondria is difficult because of their small size (down to 0.5 µm). Although microscopy may resolve larger mitochondria in cell cultures, smaller mitochondria in the retina are beyond the resolution of most optical imaging techniques. Among cellular organelles, mitochondria have been implicated as contribute significantly to light scattering.[25] Sensitivity to light scattering makes optical methods attractive for development of a candidate screening tool to detect early mitochondrial dysfunction in patients. Additionally, because the optic nerve is embryonically derived from the forebrain and encased within the meninges, the eye is now recognized by many investigators as a native "window to the brain."[26,27] In fact, considerable evidence suggests that many neurodegenerative diseases have an associated retinal pathology and diagnosis.[27–30]

Recent reports have demonstrated that optical coherence tomography (OCT) and its derivative OCT angiography (OCTA) are useful imaging tools in detecting and assessing AD. OCT was used to detect a decrease in nerve fiber layer (NFL) thickness in AD patients, and a loss of melanopsin was noted in post mortem retinal samples.[31] OCTA has also been used to identify decreased retinal vascular density in AD patients.[32,33] In addition, OCTA was used to demonstrate that AD patients have significantly reduced macular vessel density, perfusion density, and combined ganglion cell layer (GCL)–inner plexiform layer (IPL) thickness when compared to patients with pre-Alzheimer's mild cognitive impairment and controls.[34] And, profoundly, OCTA was also used to demonstrate that preclinical AD patients exhibit retinal abnormalities when compared with healthy controls, including increased foveal avascular zone and decreased inner foveal thickness.[35] Changes in microvascular perfusion will ultimately alter the mitochondrial fission–fusion state.

Although OCT is proving useful in demonstrating differences between AD, mild cognitive impairment, and control groups, contemporary OCT techniques have a limited capability to identify the earliest AD markers that may be linked to the earliest cellular/organelle changes in the retinal cell populations. Standard clinical OCT systems are not configured to resolve some of the earliest disruptions associated with the disease, including changes related to mitochondrial morphology.

Angle-resolved OCT is a subset of OCT that provides multiple signals that are sensitive to the angle of light backscattered from the specimen.[36–38] A variety of angle-resolved techniques have demonstrated the utility of incorporating angular backscattering information into the OCT signal, including multidirectional OCT for retinal imaging,[39] bright- and dark-field imaging with few-mode fibers for angular multiplexing,[40] and directional OCT for imaging melanin concentration.[41]

A specific subtype of angle-resolved OCT, termed scattering-angle-resolved OCT (SAR-OCT), positions an optical element in the pupil of the scanning system that pathlength-encodes angular information of backscattered light from the sample.[42–45] Each pupil region corresponds to a discrete optical pathlength that contains information from light that is incident or backscattered from a unique angular range. It has been demonstrated that SAR-OCT is sensitive to peripapillary variation in neuron size[44] and longitudinal changes in the hypoxic murine retina.[46]

Mouse Model of AD

A triple transgenic murine model for AD (3xTg-AD) has been utilized for AD studies. The 3xTg-AD murine model exhibits plaque and tangle pathology,[47] as well as synaptic dysfunction.[48] The onset of Aβ and tau plaques for 3xTg-AD is similar to that of AD in human patients, both age- and region-dependent.[49,50] For the 3xTg-AD murine model, Aβ immunoreactivity has been observed at 2 months in the hippocampus.[50] At 4 months, intraneuronal Aβ pathology is visible in the cortex and amygdala[51] and correlates with observable cognitive deficits.[52] At month 6, Aβ deposits are observed in the frontal cortex,[51] together with the appearance of learning deficits, memory impediments, and neophobia.[53] At 12 months, Aβ are present in the hippocampus and other cortical regions,[53] and tau immunoreactivity becomes apparent in pyramidal neurons in the CA1 region.[51]

Many AD pathologies are present in the retina (an anterior extension of the central nervous system) at varying ages in the 3xTg-AD model. In one study, retinal thickness decreased significantly, but Aβ was not detected at 4 or 8 months, although the tau levels were elevated.[54] In another study, profound tau pathology was observed in the visual system in 3xTg-AD animals as early as 3 months, prior to observation of behavioral deficits and tau accumulation in the brain.[55] The tau build-up occurred mostly in the soma and dendrites of the retinal ganglion cells (RGCs); tau depletion occurred primarily in RGC axons and the optic nerve. The morphology of Müller cells and astrocytes was examined in the 3xTg-AD retina and found to undergo complex remodeling similar to astrocyte changes in the mouse brain. Cordeiro et al.[56] showed that 14-month-old 3xTg-AD mice showed significantly more RGCs in the early stages of apoptosis and fewer necrotic cells compared to age-matched controls.

Study Aims

The aim of this study was to demonstrate that SAR-OCT is a candidate imaging approach for detecting early changes in the AD retina that go beyond vascular changes by imaging a cross-section of 3xTg-AD and control mice at various ages. The study was not designed to determine whether any observed backscattering diversity variations in the murine retina are due to specific physiologic mechanisms, such as microvascular perfusion changes, changes in mitochondrial morphology, or other cellular alterations.

Methods

This cross-sectional study used SAR-OCT to image the retinas of the 3xTg-AD murine model and age-matched control mice at four ages ranging from 10 to 48 weeks. Three imaging contrast measures were examined across this age range: (1) angiography, (2) scattering angle, and (3) retinal sublayer thickness. In the following sections, the mouse model is described, an outline of the experimental design is given, the imaging setup is presented, and collected data are reported.

Mouse Model

A triple-transgenic murine model for AD (3xTg-AD) was used for the disease model, and non-transgenic wild-type C57BL/6J mice served as controls. C57BL/6 is the background strain of Tg2576, but all C57BL/6 strains have a further designation (e.g., C57BL/6J, C57BL/6N). Because C57BL/6N is known to have a mutation for spotty retinal degeneration,[57] C57BL/6J was selected as the control; C57Bl/6J does not have the same mutation. The C57BL/6J strain has also been used as a control for Tg2576 in other studies.[58]

Taken together, then, the hypothesis for the study was that retinal changes in the 3xTg-AD mouse model compared with controls can be observed using SAR-OCT.

Experimental Design

To assess the efficacy of SAR-OCT in detecting AD in the retinas of 3xTg-AD mice compared with controls, a cross-sectional study was designed in which the retinas of 3xTg-AD mice and age-matched controls were imaged (IACUC protocol #AUP-2015-00156). The experiment adhered to the ARVO Statement for the Use of Animals in Ophthalmic and Vision Research. AD and control mice were within 3 weeks of the same age when imaged for each age group. The age and sex distribution of the 32 mice enrolled in the study (20 3xTg-AD mice and 12 age-matched C57BL/6 controls) is shown in the Table. Mice ranged in age from 10 to 48 weeks at the time of imaging. Mice were mostly male, except for the inclusion of some females in the disease group at 30 weeks (2 females) and 45 weeks (2 females).

Prior to imaging, each mouse was first anesthetized in an induction box (5% isoflurane) and then moved to the SAR-OCT imaging platform, where anesthesia continued via a custom nose cone (1.5%–3% isoflurane). The left retina was imaged using the SAR-OCT

Table. Study Enrollment Included 20 3xTg-AD Mice and 12 Age-Matched Controls for SAR-OCT Retinal Imaging

Group	Control Mice ($n = 12$)	3xTg-AD Mice ($n = 20$)
Group 1 (10 wk)	10 wk old (3 males)	10 wk old (5 males)
Group 2 (20 wk)	19 wk old (3 males)	22 wk old (2 males)
Group 3 (30 wk)	29 wk old (3 males)	30 wk old (2 males, 2 females)
Group 4 (45 wk)	46 wk old (3 males)	45 wk old (2 males, 2 females)
		48 wk old (5 males)

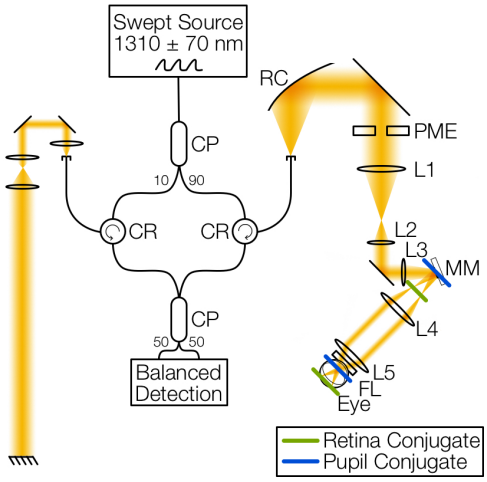

Figure 1. The SAR-OCT instrument for murine retinal imaging includes a 1310 ± 70 nm swept-source laser and a fiber-based Mach–Zehnder interferometer. The sample arm includes a reflective collimator (RC), pathlength multiplexing element (PME), several gradient index lenses (L1–L5), a dual-axis microelectromechanical system (MEM) mirror conjugated to the ocular pupil plane, and a fundus lens (FL) that interfaces with the mouse cornea. The reference arm includes three lenses for dispersion compensation and a mirror path length matched to the retina of the mouse. CP, fiber coupler; CR, fiber circulator. Reproduced with permission from Gardner et al.[42]

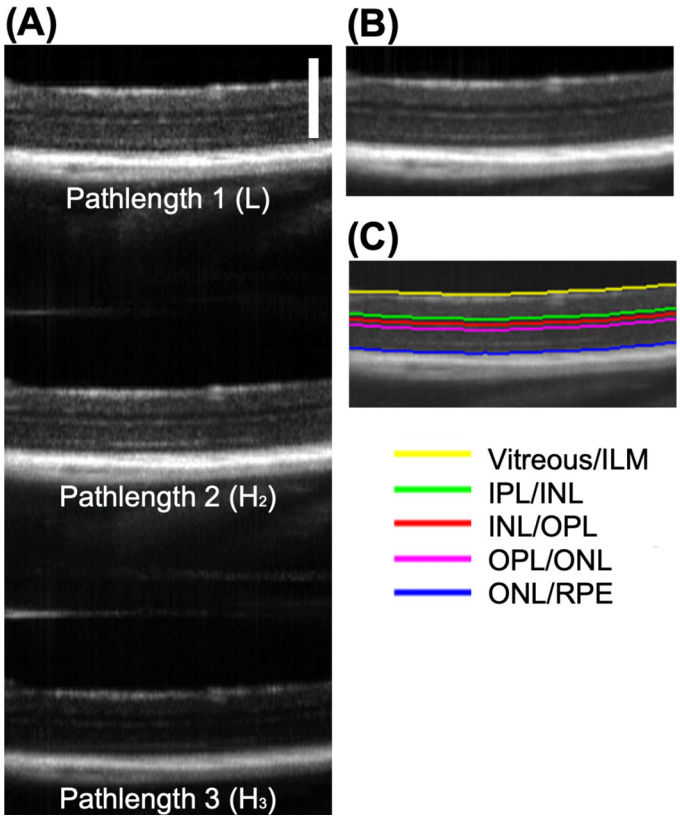

Figure 2. (A) Native path length multiplexed SAR-OCT image contains three sub-images, each with a different path length (L, H2, and H3). (B) Eight repeating B-scans collected for angiography are averaged and displayed as a single OCT retinal image in logarithmic scale. (C) The averaged retinal image is segmented using a custom semiautomatic algorithm. The axial scale bar is 300 µm; the lateral field of view is 1.3 mm (37°). Signal amplitude in pathlengths 1 and 2 are maximized and balanced to encode more discernable scattering information. ILM, internal limiting membrane; INL, inner nuclear layer; OPL, outer plexiform layer; RPE, retinal pigment epithelium. Reproduced with permission from Gardner et al.[46]

murine imaging system for about 15 minutes, and then the mouse was allowed to recover. For each mouse an imaging session required around 30 minutes.

SAR-OCT Instrumentation

SAR-OCT instrumentation (Fig. 1) used for this study was previously described in detail by Gardner et al.[43] A pathlength multiplexing element (PME) is introduced into the sample path at a position conjugate to the murine ocular pupil plane, and the PME encodes light scattered at lower and higher angles into three different pathlengths (Fig. 2). The SAR-OCT instrument utilizes a swept-source laser (1310 ± 70 nm; 100-kHz sweep rate) manufactured by Axsun, Inc. (Billerica, MA). The cornea is index-matched to the objective lens, and the ocular pupil is conjugated to the microelectromechanical systems scanning mirror in order to maximize the scan region of the retina accessible by the SAR-OCT system. The beam is focused through the length of the mouse eye, already having some optical power upon entering. At the first surface of the cornea, the beam diameter is 0.7 mm. Given the axial length of the first cornea surface to the retina (3.3 mm in our model) and the weighted average of

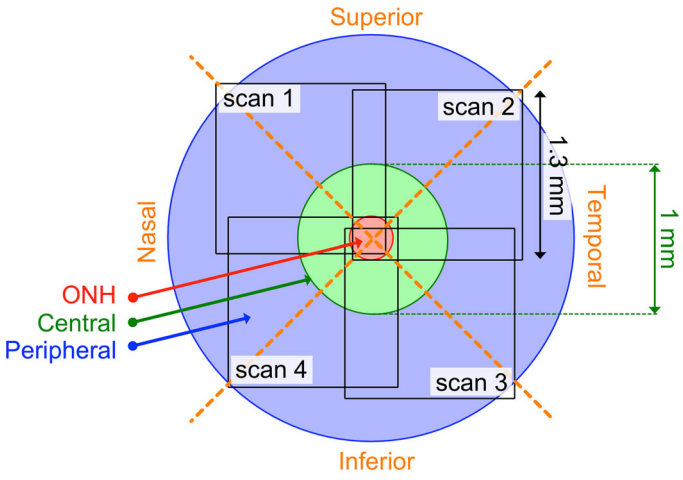

Figure 3. Murine retina was scanned four times, each scan containing a segment of the ONH in a 1.3 × 1.3-mm^2 square. The central region is defined by a 1-mm-diameter circle centered on the ONH. The peripheral retina is any area outside of the central region. Only left eyes were imaged in this study. Retinal images are segmented into four azimuthal regions: nasal, superior, temporal, and inferior.

the index of refraction at 1310 nm (1.52),[43] the airy disk spot size is 24 µm and matches the value from the Zemax model (Zemax Development Corp., Kirkland, WA). The imaging system has an axial resolution of 11.7 µm in air, and the SAR-OCT imager is capable of detecting changes in bulk scattering angle up to 8° from a direct backscatter (0°).[43]

Data Collected

Several SAR-OCT images were collected from each mouse retina over different regions of interest to obtain an expansive view of the retina. Under typical imaging conditions, the optic nerve head (ONH) was placed once in each corner of the en face view so we could collect four volumes with different regions of the same retina with minimal overlap. Occasionally, animal care constraints limited the number of volume acquisitions, and four volumes could not be collected. From one to four retinal volumes were recorded for each mouse. Each square area imaged was 1.3 mm × 1.3 mm (512 × 512 A-scans). Figure 3 shows a schematic of the various imaging regions. Further sample B-scans are included in the Supplementary Material (Supplementary Figs. S1, S2).

Angiography

At each of the four scan locations, eight B-scans were recorded sequentially, enabling angiographic data to be computed via a complex differential variance algorithm[59,60] across a large section of the retina. After flattening the three plexuses into three images (superficial, intermediate, and deep) based on the segmentation boundaries, each of the images was filtered using Frangi filtering.[61] The Frangi filter uses the derivative of two-dimensional Gaussian distributions with user-defined widths to search for vessel-like features. Four scaling values (Gaussian widths) were chosen to match the range of murine vessel widths in the retina: 3.2 µm, 17.4 µm, 31.6 µm, and 45.8 µm[62] (approximately 1, 7, 13, and 18 pixels, respectively).

After Frangi filtering, an adaptable threshold was applied to angiography images to define vascular and non-vascular regions. Based on Bradley's method,[63] the MATLAB (MathWorks, Natick, MA) function "adaptthresh" automatically selected a threshold for every pixel based on local mean intensity in the neighborhood of that pixel. The automatic selected threshold was tuned with a heuristically selected sensitivity parameter (0.2), which was used for all images.

Vascular density (VD) has been defined as the fractal dimension of the vasculature,[32] using the box counting method. We also examined VD as a fractal dimension, and we determined the percent volume occupied by blood flow. Angiography features (Supplementary Table S1) were explored across all vascular plexus (superficial, intermediate, and deep) and across central and peripheral retinal regions (ONH, as reference). All retinal regions examined are tabulated in the Results section.

Scattering

To examine scattering contrast, we computed the ratio (L/H_2) of intensities in pathlength 1 (L) and pathlength 2 (H_2) images. Each voxel in a defined region was treated as a sample, and a Burr type XII distribution was fitted to the normalized histogram of the distribution of ratios. Three parameters of the Burr type XII distribution (α, C, and K) were optimized to minimize error between the normalized histogram and the fitted distribution. See Gardner et al.[46] for a more complete description of the Burr type XII distribution applied to fit the histogram of L/H_2 ratios.

The fitted C parameter has been found to yield meaningful insight into tissue scattering properties imaged with SAR-OCT.[46] Qualitatively, the C parameter represents the variance of the Burr type XII distribution. Accordingly, to examine scattering differences, mice were compared across disease status (AD vs. control) and across age using a series of Wilcoxon rank-sum tests. Differences by (1) retinal layers and (2) vascular compared with non-vascular tissue regions were determined (all regions are tabulated in the Results section). Vascular regions were determined by masking the layers based on thresholded angiographic data, collected with each scan.

Retinal Layer Thickness

SAR-OCT images were utilized to compare thicknesses of various retinal sublayers in different regions for disease and control groups at each measured time point (exact regions tabulated in the Results section). Thickness measurements are not unique SAR-OCT features but are commonly used clinically to detect various diseases. Retinal sublayer thicknesses were obtained using a retinal segmentation algorithm outlined in Gardner et al.[43]

Correlation Between the C Parameter and Retinal Thickness

A topic of interest is the relationship between retinal thickness and the C parameter. If the C parameter does not provide independent information, then SAR-OCT might be a redundant tool for early detection of AD, where standard thickness measurements would be a comparable marker of disease state. To investigate the relationship between retinal thickness and the C parameter, Spearman's correlation coefficient was calculated. Spearman's correlation makes no distributional assumptions and is thus appropriate for the limited non-parametric data collected in this pilot study. We compared the rank order of the retinal layers (superficial layers, inner nuclear layer, outer plexiform layer, and outer nuclear layer) to the rank order of the corresponding C parameters to test for a monotonic trend. The presence of a trend would indicate that the C parameter might be a redundant measure.

Results

Nonparametric Wilcoxon rank-sum test results comparing 3xTg-AD and control mice versus age are plotted in Figures 7 to 10 and tabulated comprehensively in the Supplementary Material. The Spearman correlation data are presented in Figure 11.

Angiography

Based on the angiography images (Fig. 4), two features (A3 and A12) showed statistically significant differences at 29 to 30 weeks (Supplementary Table S1). Two other features (A10 and A11) were close to significance with P values near 0.05. At the latest time point (45–48 weeks), no differences were noted.

Scattering

Figure 5 shows an example segmented L/H_2 B-scan displayed alongside a corresponding segmented and unsegmented B-scan (see also Supplementary Fig. S3). For the C parameter (a measure of spread of L/H_2 for a three-dimensional region of interest within a retinal layer), statistical differences between the 3xTg-AD mice and the control mice were prominent as early as 10 weeks and persisted through all ages for various retinal sublayers (Supplementary Table S2). Example AD and control L/H_2 distributions and Burr fits are shown in Figure 6.

Five of 15 layer/region combinations revealed significantly higher C parameters in the control mice at 10 weeks and 30 weeks: features S2, S3, S10, S11, and S15 (Figs. 7, 8; Supplementary Table S2). Significant differences were largely in the superficial layers, specifically the NFL and the GCL. Generally, the C parameters of both control and AD groups decreased with increasing mouse age. C parameters of the control group tended to decrease more rapidly with age compared to those for the AD group, which exhibited lower C parameters at early ages. The C parameters for the control group generally decreased with time, but

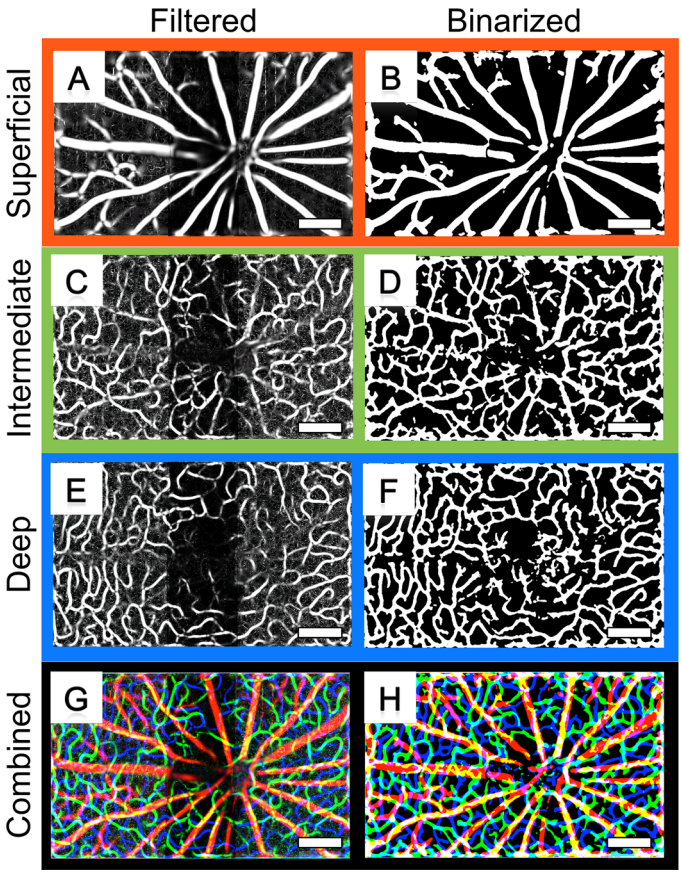

Figure 4. Exemplary angiography images. Images collected from mouse 4 in the 10-week-old AD group include images after Frangi filtering (A, C, E, G) and before binarization (B, D, F, H). (G, H) An RGB colorized image where red represents superficial, green intermediate, and blue deep plexuses. *Scale bars* (*bottom right*): 300 µm.

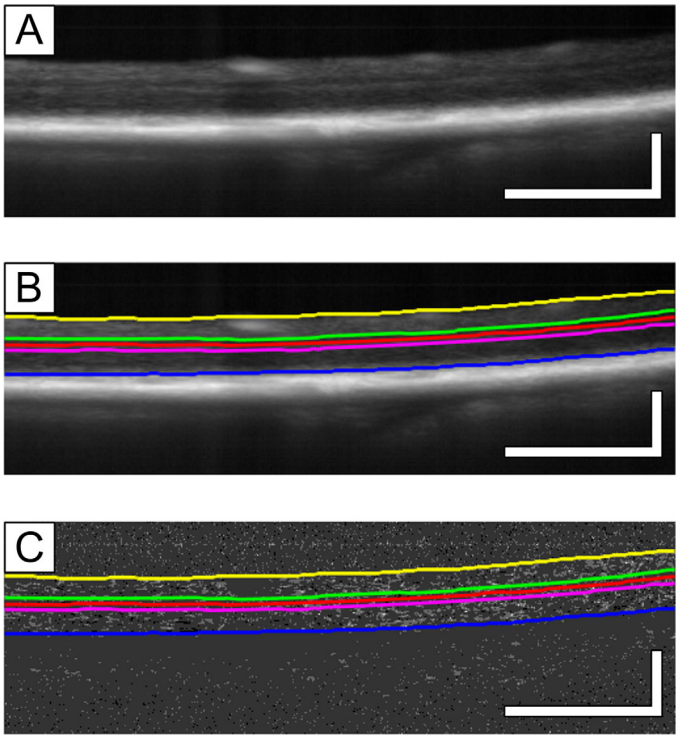

Figure 5. Exemplary B-scans (same location) selected from mouse 3 in the 45-week-old AD group. (A) Unsegmented B-scans (30 B-scans averaged); (B) same B-scan locations, segmented; and (C) L/H_2 values in the same B-scan locations, segmented. Boundary colors match those in Figure 2. *Scale bars*: 300 µm.

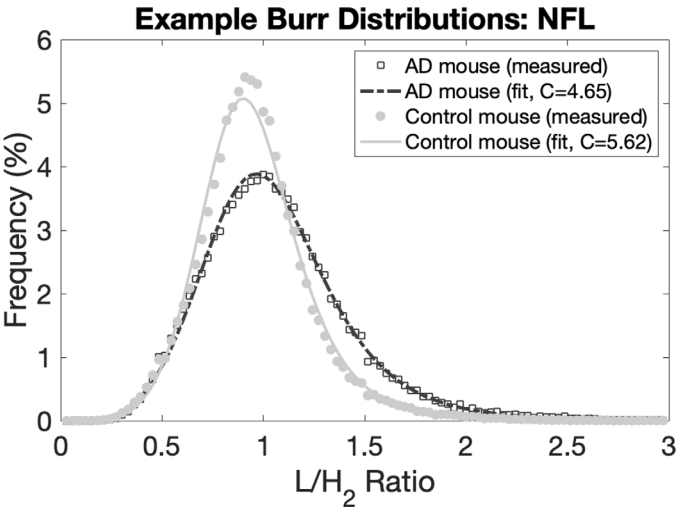

Figure 6. Nerve fiber layer L/H_2 probability density functions for one AD mouse and one control mouse in the 10-week-old age group. The fitted probability density functions are displayed over the raw data. The AD mouse has a lower C parameter (4.65) than the control mouse (5.62) in the NFL. The C parameter is inversely related to the spread of the function.

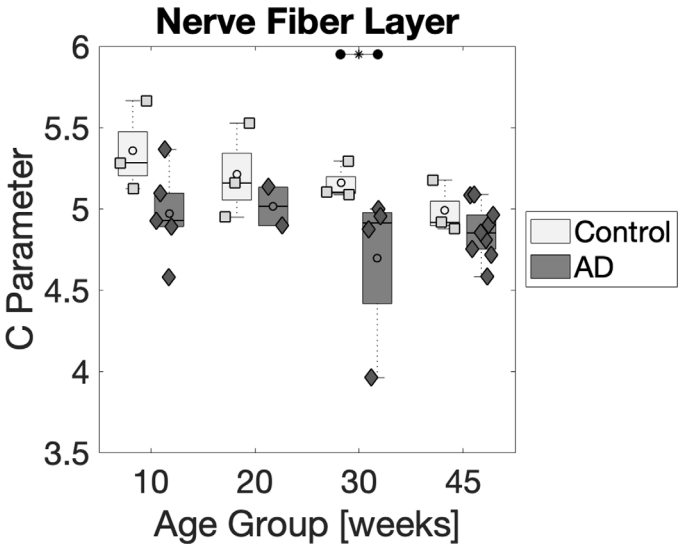

Figure 7. Distribution of C parameters in the NFL for combined vascular and non-vascular zones (feature S2) shows statistical differences between control and AD groups at 10 weeks. Center circles represent mean; middle line, median; bars, standard deviation; outside lines, minimum/maximum. Individual measurements are overlaid with squares (control group) and diamonds (AD group). Larger differences in mean across groups are apparent in the earliest time points, although statistical significance is only obtained at 30 weeks. Lines at the top of the figure with an asterisk (*) indicate $P < 0.05$ for one-sided Wilcoxon rank-sum tests.

the C parameters for the AD group began at a lower value and had a smaller rate of change with increasing animal age.

Retinal Layer Thickness

Example segmented layers are displayed in Figures 5B and 5C. Differences in retinal layer thicknesses between the control and 3xTg-AD groups were largely isolated to superficial layers (retinal NFL + GCL + IPL) and the ONL, with differences also appearing in total retinal thickness (Supplementary Table S3). Central retinal regions showed the most consistent thickness differences between the control and 3xTg-AD groups. The mean central superficial layer was thicker in control mice at every age, significantly so at 10 and 30 weeks (Fig. 9). Similarly, mean total retinal thickness in the central retinal zones was greater in the control group at every age, significantly so at 10 and 30 weeks (Fig. 10).

Correlation Between C-Parameter and Retinal Thickness

The Spearman rank-sum correlation test revealed very low correlation between retinal sublayer

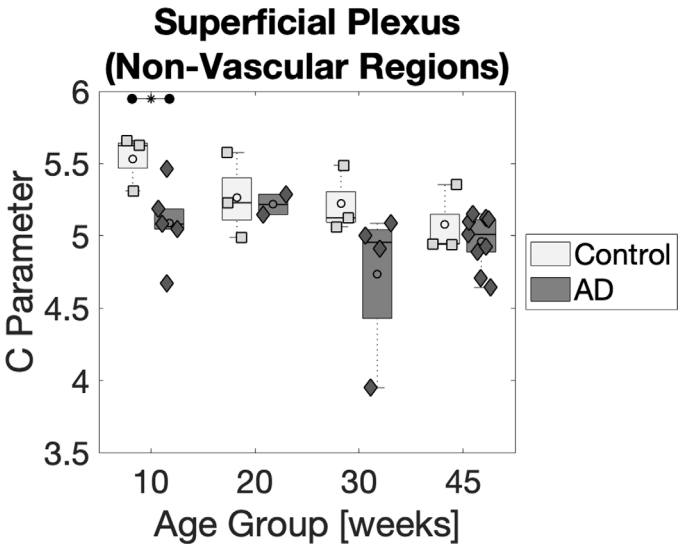

Figure 8. Distribution of C parameters in non-vascular superficial layers (feature S11) shows statistical differences between the AD and control groups at 10 weeks. Lines at the top of the figure with an asterisk (*) indicate $P < 0.05$ for Wilcoxon rank-sum tests.

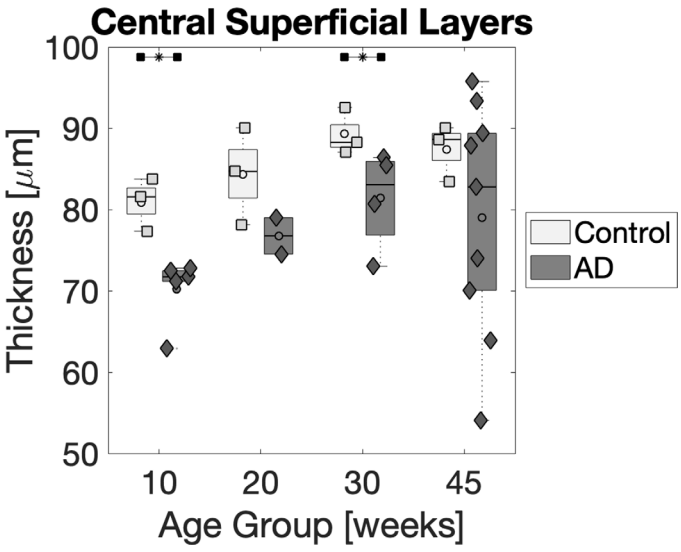

Figure 9. Central superficial retinal thickness (feature T2) for AD and control mice. Significant differences are apparent between the AD and control groups at 10 and 30 weeks. The mean thickness is greater for control mice at all time points. Lines at the top of the figure with an asterisk (*) indicate $P < 0.05$ for one-sided Wilcoxon rank-sum tests.

thicknesses and C parameters. Each of the correlation coefficients was nearly zero, and none of the P values was less than $\alpha = 0.05$ (Fig. 11). These results suggest that the SAR-OCT C parameter is an independent measure from the retinal sublayer thicknesses that standard OCT provides.

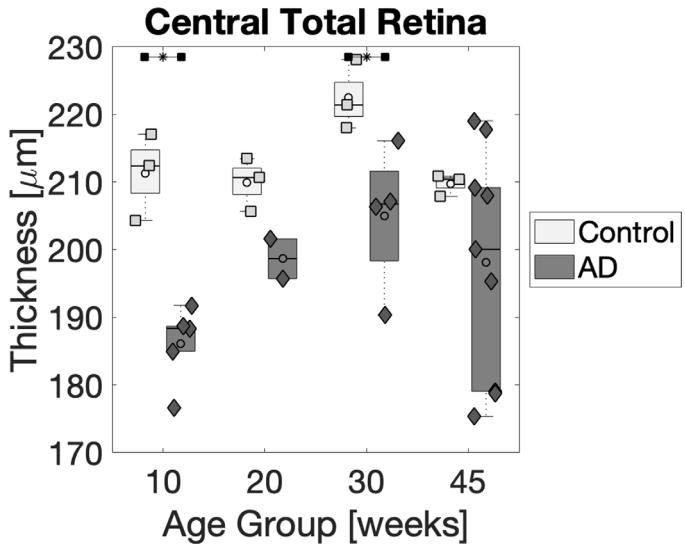

Figure 10. Central total retinal thickness (feature T14) for AD and control mice. Significant differences are apparent between the AD and control groups at 10 and 30 weeks. Lines at the top of the figure with an asterisk (*) indicate $P < 0.05$ for one-sided Wilcoxon rank-sum tests.

Discussion

The C parameter derived from the SAR-OCT images demonstrated sensitivity to distinguishing differences between control and 3xTg-AD mice. Our original hypothesis was that differences in retinal scattering might only be apparent in older animals; however, the data show that differences in the scattering properties and layer thickness are apparent at young ages and differences can persist as the animals become older.

Angiography

Interestingly, SAR-OCT retinal imaging and subsequent image analysis for 3xTg-AD mice did not identify significant differences in vascular structure as measured by fractal analysis (for VD) or by percent blood volume; however, differences may have been present but not identified, given that other studies have found vasculature changes in the macula. Possibilities are that either vascular changes did not occur at the measured time points in this model or the SAR-OCT system employed in this study was insensitive to changes in perfusion.

The SAR-OCT system used in this study was optimized for scattering angle detection, including a large numerical aperture objective for better angular discrimination. One trade-off of this approach is that the depth of focus is reduced, so that some retina layers

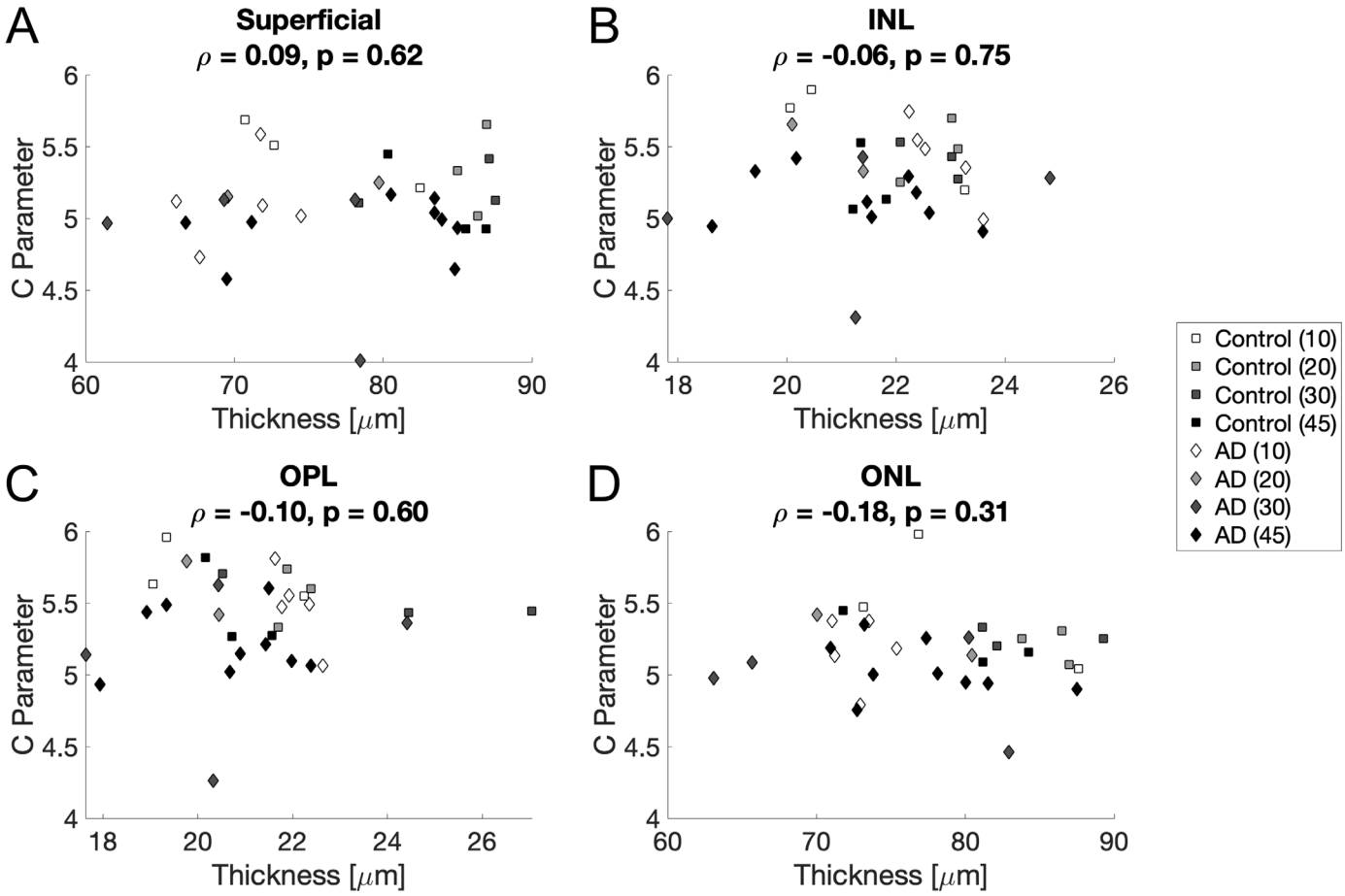

Figure 11. Spearman rank-sum correlation test results indicate little correlation between retinal layer thicknesses and C parameters: (A) superficial layers, (B) inner nuclear layer (INL), (C) outer plexiform layer (OPL), and (D) outer nuclear layer (ONL). ρ is the correlation coefficient (all close to 0); no *P* values were less than $\alpha = 0.05$.

may be out of focus. Although the focal plane position was kept as consistent as possible between mice, thus maintaining data integrity to indicate differences in scattering angle, decreased lateral resolution in the deep vascular plexus could have limited detection of vascular differences, if present.

Scattering

The authors previously observed a decrease in the retinal C parameter with ischemic cell death, and the largest change in the C parameter during ischemia was observed in non-vascular regions.[46] A hypothesis is that increasing morphological disorganization in the retina due to energy loss is a major cause of the observed decrease in the C parameter (i.e., increase in scattering diversity). For 3xTg-AD retinas, scattering changes may arise from one or more of the following: (1) overexpression of Aβ precursor protein, Aβ, and/or tau deposition; (2) neuronal cell loss; (3) retinal glial cell changes, or (4) vascular changes.

Increased rates of mitochondria-initiated apoptosis also lead to a decrease in cell density, particularly in RGCs,[30] and thus contribute to lower cellular uniformity. Taken together, mitochondrial morphology may be a contributing factor in observed differences between the 3xTg-AD model and control groups. Without extensive ultrastructural analysis of murine retinas, identifying the morphological causes of scattering angle changes is challenging.

Another interesting finding in the present study is the progressive decrease of the C parameter with increasing mouse age. This hypothesis was tested using one-way ANOVA, which indicated that the C parameter for several retinal regions and layers did, in fact, decrease with age (C parameter for 45 weeks less than C parameter for 10 weeks; $P < 0.05$). This observed decrease in the C parameter may be due to decreased cellular and synaptic density in the retina.

Additional retinal changes that are associated with age are reflected in the scattering data (C parameter). As the animal ages, the RGCs become less dense.[64] Fewer synaptic connections are present in any given IPL volume of older mouse retinas, and the area of RGC dendritic and axonal arbors decreases.[64] Overall, a general decrease in cellular and synaptic density occurs as the mouse ages.[64] The C parameter also decreases with mouse age in both groups (e.g., Figs. 7, 8). A decrease in cellular density is a candidate mechanism that may impact decreases in the C parameter.

Thickness

Statistically significant differences in retinal sublayers between 3xTg-AD mice and controls mice are generally isolated to two regions: (1) the superficial layers (NFL + GCL + IPL) and (2) the ONL. The NFL, IPL, and outer plexiform layer are the three murine sublayers that contain most of the synapses of the retina; other retinal layers are dominated by cell bodies. Inasmuch as AD is known to affect the synapses in early disease states, observed changes in the NFL and IPL are consistent with the known pathophysiology of AD. The SAR-OCT system and segmentation algorithm employed here were unable to segment out the NFL precisely, so conclusions cannot be drawn as to whether observed changes in combined superficial layers are due to the NFL, GCL, and/or IPL.

Differences in total retinal thickness observed in this study are consistent with published histological data from Liu et al.,[65] who also reported a decrease in the Tg2576 total retinal thickness when compared to wild-type controls. The magnitude of the difference observed in the present study is less than that reported by Liu et al., but that may be due to differences in experimental methods. Liu et al. reported total retinal thickness as an average of only four manually measured distances from histological data. (We have previously reported rapid post mortem changes in retinal thickness.[46]) Liu et al. reported mean total retinal thickness in wild-type controls as 246 µm and mean total retinal thickness in Tg2576 mice as 156 µm. In the present study, for the oldest mice and entire retina (which are the best comparisons to the Liu et al. dataset), control animals had a mean total retinal thickness of 208 µm and 196 µm for Tg2576 as measured by SAR-OCT. Total retinal thickness is taken as the physical distance from the vitreous/internal limiting membrane boundary to the ONL/retinal pigment epithelium boundary, and the refractive index of the retina is assumed to be 1.38 at 1310 nm, based on the Conrady dispersion[66] fit of Remtullah's refractive index measurements.[67] Total retinal thickness data from the present study are consistent with those of Liu et al.,[65] and variations may be due to methodological differences.

Our approach to measure retinal thickness was manifestly different than that employed by Liu et al.[65] in that we considered the automatically detected thickness at every SAR-OCT A-scan location in the retina. Images were then divided into central and peripheral regions of interest for higher dimensional analysis. Robustness of the reported approach reduces the possibility of unintended bias in region of interest selection.

Differences among age groups within the AD and control groups are noteworthy. The murine retina thins (axially) at lateral positions in older mice while maintaining volume.[24] Mice imaged in this study exhibited mean retinal sublayer thicknesses slightly greater at older ages (AD and control groups), although not significantly ($P > 0.05$, Wilcoxon rank-sum test). The authors note that the present study does not suggest that older mice have thicker retinas than younger mice; indeed, statistical analysis of the data does not support such a claim. Numerous clinical studies observe thinner retinas in older human subjects, particularly in the parapapillary retinal fiber layer.[68–72]

Polarization

This work did not explore differences in birefringence-induced phase retardation between control and 3xTg-AD mice; however, one may hypothesize that polarization-sensitive OCT (PS-OCT) may provide contrast analogous to SAR-OCT. More specifically, because light depolarization is due to scattering, higher degrees of depolarization measured by PS-OCT might scale with a derived SAR-OCT parameter. To test this hypothesis, additional studies that directly compare PS-OCT and SAR-OCT should to be completed.

In a similar cross-sectional pilot study, Harper et al.[73] used multi-contrast OCT (standard reflectivity data, PS data, and OCT angiograms) to examine the retinas of a transgenic AD mouse model. Their study compared 24 APP/PS1 transgenic mice (age, 45–104 weeks) and 15 age-matched controls. The results indicate that observed birefringence-induced phase retardation abnormalities were not associated with Aβ plaques in the retina (instead with melanin migration), and there was no apparent difference between the AD and control groups in this regard. Whereas the transgenic mouse model employed by Harper et al. is different than that employed in this study, a comparison of the results of these studies suggests that SAR-OCT is

sensitive to a retinal scattering signal that is distinct from polarimetric-based signals detected with PS-OCT.

Limitations

This study is limited by at least two factors. First, because this work is a cross-sectional study, the ability to draw more definitive conclusions is limited; however, the significance of the results and potential implications should not be easily dismissed. Significant scattering differences between the AD and control groups were detected in the scattering in both the 10-week and 30-week cohorts. However, careful examination of the data suggests that a more extensive longitudinal study with the same mouse model may reveal significant differences at other ages. As noted in the results section, the mean C parameter for almost all AD age groups was lower than the mean C parameter for control mice of the same age. By increasing the number of mice studied, differences in the C parameter are expected to become more statistically meaningful. In general, cross-sectional studies provide impetus for further study, as has been established here. The results of this study warrant further examination of the scattering properties of the retina for AD detection, as well as the utility of SAR-OCT and related optical methods to that end.

Second, the resolution of the SAR-OCT system did not allow for NFL segmentation. Other similar studies have also been unable to segment out the NFL in mice.[73] Still, quantifiable patterns are present in superficial layers. Furthermore, each mouse volume was manually inspected in five B-scan locations to ensure the accuracy of the segmentation algorithm. Volumes with segmentation errors were segmented again with more manual control over the boundary detection to ensure accuracy.

Given these limitations, the authors do not believe that the results of the C parameter changes would be modified should a SAR-OCT system with better resolution be utilized to conduct the study.

Translation

SAR-OCT provides a novel and clinically translatable avenue to search for early stage biomarkers for neurodegeneration. The results of this cross-sectional study provide a basis to motivate future studies in larger animals and ultimately humans. Depending on the coherence length of the tunable laser source, addition of a PME (glass element with center aperture) can potentially convert a clinical OCT system into an SAR-OCT system, thus making human trials tractable.

Conclusions

In this pilot study, 3xTg-AD mouse retinas were observed to have significant differences in scattering properties and retinal sublayer thicknesses when compared to non-transgenic wild-type C57BL/6J control mice in a cross-sectional study. The 3xTg-AD mice had greater scattering diversity (lower C parameter) than the control mice—in many retinal sublayers—at the earliest ages examined (10 weeks). Scattering diversity increased with age (apparent in both AD and control models) and at a faster rate in control mice such that scattering differences between control and 3xTg-AD mice were not detectable with SAR-OCT in the oldest animals studied (45 weeks). Thicknesses of the total retina and superficial layers alone were less in the 3xTg-AD model than the thicknesses of those same layers in controls at every measured time point. With the SAR-OCT system employed here, no differences were detected in vascular density or in the percent volume occupied by blood flow. SAR-OCT is a demonstrated candidate tool for early detection of AD by means of scattering angle variation. Further studies are required to determine whether the scattering properties of retinal sublayers may be helpful to detect and classify the state of neurodegeneration in humans.

Acknowledgments

Supported by a grant from The University of Texas System Neuroscience and Neurotechnology Research Institute and the Cancer Prevention Research Institute of Texas (DP 150102). MRG and VB were supported by a National Institutes of Health T32 Institutional Training Grant (EB007507), and VB was supported by a National Institutes of Health Big Data to Knowledge (BD2K) Grant (LM012414-01A1).

Disclosure: **M.R. Gardner,** None; **V. Baruah,** None; **G. Vargas,** None; **M. Motamedi,** None; **T.E. Milner,** None; **H.G. Rylander,** None

References

1. Alzheimer's Association 2016 Alzheimer's disease facts and figures. *Alzheimers Dement 2016*. 2016;12:459–509.
2. Hebert LE, Weuve J, Scherr PA, Evans DA. Alzheimer disease in the United States (2010-2050)

estimated using the 2010 census. *Neurology*. 2013;80:1778–1783.
3. Siegel R, Ma J, Zou Z, Jemal A. Cancer statistics, 2014. *CA Cancer J Clin*. 2014;64:9–29.
4. Albert MS, DeKosky ST, Dickson D, et al. The diagnosis of mild cognitive impairment due to Alzheimer's disease: recommendations from the National Institute on Aging-Alzheimer's Association workgroups on diagnostic guidelines for Alzheimer's disease. *Alzheimer's Dement*. 2016;7:270–279.
5. Sperling RA, Aisen PS, Beckett LA, et al. Toward defining the preclinical stages of Alzheimer's disease: recommendations from the National Institute on Aging-Alzheimer's Association workgroups on diagnostic guidelines for Alzheimer's disease. *Alzheimers Dement*. 2011;7:280–292.
6. Jack CR, Knopman DS, Jagust WJ, et al. Update on hypothetical model of Alzheimer's disease biomarkers. *Lancet Neurol*. 2013;12:207–216.
7. Villemagne VL, Burnham S, Bourgeat P, et al. Amyloid β deposition, neurodegeneration, and cognitive decline in sporadic Alzheimer's disease: a prospective cohort study. *Lancet Neurol*. 2013;12:357–367.
8. Reiman EM, Quiroz YT, Fleisher AS, et al. Brain imaging and fluid biomarker analysis in young adults at genetic risk for autosomal dominant Alzheimer's disease in the presenilin 1 E280A kindred: a case-control study. *Lancet Neurol*. 2012;11:1048–1056.
9. Jack CR, Lowe VJ, Weigand SD, et al. Serial PIB and MRI in normal, mild cognitive impairment and Alzheimer's disease: implications for sequence of pathological events in Alzheimer's disease. *Brain*. 2009;132:1355–1365.
10. Mueller SG, Weiner MW, Thal LJ, et al. Ways toward an early diagnosis in Alzheimer's disease: the Alzheimer's Disease Neuroimaging Initiative (ADNI). *Alzheimers Dement*. 2005;1:55–66.
11. Liu-Seifert H, Siemers E, Holdridge KC, et al. Delayed-start analysis: mild Alzheimer's disease patients in solanezumab trials, 3.5 years. *Alzheimers Dement (N Y)*. 2015;1:111–121.
12. Brookmeyer R, Johnson E, Ziegler-Graham K, Arrighi HM. Forecasting the global burden of Alzheimer's disease. *Alzheimers Dement*. 2007;3:186–191.
13. Perl DP. Neuropathology of Alzheimer's disease. *Mt Sinai J Med*. 2010;77:32–42.
14. Selkoe DJ. Alzheimer's disease is a synaptic failure. *Science*. 2002;298:789–791.
15. Du H, Guo L, Yan S, Sosunov AA, McKhann GM, Yan SS. Early deficits in synaptic mitochondria in an Alzheimer's disease mouse model. *Proc Natl Acad Sci USA*. 2010;107:18670–18675.
16. Wu HY, Hudry E, Hashimoto T, et al. Amyloid β induces the morphological neurodegenerative triad of spine loss, dendritic simplification, and neuritic dystrophies through calcineurin activation. *J Neurosci*. 2010;30:2636–2649.
17. Wang X, Su B, Lee HG, et al. Impaired balance of mitochondrial fission and fusion in Alzheimer's disease. *J Neurosci*. 2009;29:9090–9103.
18. Swerdlow RH, Burns JM, Khan SM. The Alzheimer's disease mitochondrial cascade hypothesis: progress and perspectives. *Biochim Biophys Acta*. 2014;1842:1219–1231.
19. Oddo S, Billings L, Kesslak JP, Cribbs DH, LaFerla FM. Abeta immunotherapy leads to clearance of early, but not late, hyperphosphorylated tau aggregates via the proteasome. *Neuron*. 2004;43:321–332.
20. Ohyagi Y, Asahara H, Chui D-H, et al. Intracellular Abeta42 activates p53 promoter: a pathway to neurodegeneration in Alzheimer's disease. *FASEB J*. 2005;19:255–257.
21. Suo Z, Cox AA, Bartelli N, et al. GRK5 deficiency leads to early Alzheimer-like pathology and working memory impairment. *Neurobiol Aging*. 2007;28:1873–1888.
22. Han XJ, Hu YY, Yang ZJ, et al. Amyloid β-42 induces neuronal apoptosis by targeting mitochondria. *Mol Med Rep*. 2017;16:4521–4528.
23. Desagher S, Martinou JC. Mitochondria as the central control point of apoptosis. *Trends Cell Biol*. 2000;10:369–377.
24. Gross A, McDonnell JM, Korsmeyer SJ. BCL-2 family members and the mitochondria in apoptosis. *Genes Dev*. 1999;13:1899–1911.
25. Mourant JR, Freyer JP, Hielscher AH, Eick AA, Shen D, Johnson TM. Mechanisms of light scattering from biological cells relevant to noninvasive optical-tissue diagnostics. *Appl Opt*. 1998;37:3586–3593.
26. Maresca A, la Morgia C, Caporali L, Valentino ML, Carelli V. The optic nerve: a "mito-window" on mitochondrial neurodegeneration. *Mol Cell Neurosci*. 2013;55:62–76.
27. London A, Benhar I, Schwartz M. The retina as a window to the brain - from eye research to CNS disorders. *Nat Rev Neurol*. 2013;9:44–53.
28. Petzold A, de Boer JF, Schippling S, et al. Optical coherence tomography in multiple sclerosis: a systematic review and meta-analysis. *Lancet Neurol*. 2010;9:921–932.

29. Archibald NK, Clarke MP, Mosimann UP, Burn DJ. The retina in Parkinson's disease. *Brain*. 2009;132:1128–1145.
30. Guo L, Duggan J, Cordeiro MF. Alzheimer's disease and retinal neurodegeneration. *Curr Alzheimer Res*. 2010;7:3–14.
31. La Morgia C, Ross-Cisneros FN, Koronyo Y, et al. Melanopsin retinal ganglion cell loss in Alzheimer disease. *Ann Neurol*. 2016;79:90–109.
32. Jiang H, Wei Y, Shi Y, et al. Altered macular microvasculature in mild cognitive impairment and Alzheimer disease. *J Neuroophthalmol*. 2018;38:292–298.
33. Bulut M, Kurtuluş F, Gözkaya O, et al. Evaluation of optical coherence tomography angiographic findings in Alzheimer's type dementia. *Br J Ophthalmol*. 2018;102:233–237.
34. Yoon SP, Grewal DS, Thompson AC, et al. Retinal microvascular and neurodegenerative changes in Alzheimer's disease and mild cognitive impairment compared with control participants. *Ophthalmol Retin*. 2019;3:489–499.
35. O'Bryhim BE, Apte RS, Kung N, Coble D, Van Stavern GP. Association of preclinical Alzheimer disease with optical coherence tomographic angiography findings. *JAMA Ophthalmol*. 2018;136:1242–1248.
36. Wax A, Yang C, Backman V, et al. Cellular organization and substructure measured using angle-resolved low-coherence interferometry. *Biophys J*. 2002;82:2256–2264.
37. Kim S, Heflin S, Kresty LA, et al. Analyzing spatial correlations in tissue using angle-resolved low coherence interferometry measurements guided by co-located optical coherence tomography. *Biomed Opt Express*. 2016;7:1400.
38. Terry N, Zhu Y, Thacker JKM, et al. Detection of intestinal dysplasia using angle-resolved low coherence interferometry. *J Biomed Opt*. 2011;16:106002.
39. Wartak A, Augustin M, Haindl R, et al. Multidirectional optical coherence tomography for retinal imaging. *Biomed Opt Express*. 2017;8:5560–5578.
40. Eugui P, Lichtenegger A, Augustin M, et al. Beyond backscattering: optical neuroimaging by BRAD. *Biomed Opt Express*. 2018;9:2476–2494.
41. Meleppat RK, Zhang P, Ju MJ, et al. Directional optical coherence tomography reveals melanin concentration-dependent scattering properties of retinal pigment epithelium. *J Biomed Opt*. 2019;24:1–10.
42. Gardner MR, Katta N, McElroy A, Baruah V, Rylander HG, Milner TE. Scattering angle resolved optical coherence tomography for in vivo murine retinal imaging. *P*roc SPIE. 2017;10053:100531O.
43. Gardner M, Katta N, Rahman A, Rylander H, Milner T. Design considerations for murine retinal imaging using scattering angle resolved optical coherence tomography. *Appl Sci*. 2018;8:2159.
44. Wang B, Yin B, Dwelle J, Rylander HG, Markey MK, Milner TE. Path-length-multiplexed scattering-angle-diverse optical coherence tomography for retinal imaging. *Opt Lett*. 2013;38:4374–4377.
45. Yin B, Dwelle J, Wang B, et al. Fourier optics analysis of phase-mask-based path-length-multiplexed optical coherence tomography. *J Opt Soc Am A Opt Image Sci Vis*. 2015;32:2169–2177.
46. Gardner MR, Rahman AS, Milner TE, Rylander HG, III. Scattering-angle-resolved optical coherence tomography of a hypoxic mouse retina model. *J Exp Neurosci*. 2019;13:1179069519837564.
47. Hsiao K, Chapman P, Nilsen S, et al. Correlative memory deficits, Abeta elevation, and amyloid plaques in transgenic mice. *Science*. 1996;274:99–102.
48. Oddo S, Caccamo A, Shepherd JD, et al. Triple-transgenic model of Alzheimer's disease with plaques and tangles: intracellular Aβ and synaptic dysfunction. *Neuron*. 2003;39:409–421.
49. Mesulam M. A plasticity-based theory of the pathogenesis of Alzheimer's disease. *Ann N Y Acad Sci*. 2000;924:42–52.
50. Mastrangelo MA, Bowers WJ. Detailed immunohistochemical characterization of temporal and spatial progression of Alzheimer's disease-related pathologies in male triple-transgenic mice. *BMC Neurosci*. 2008;9:81.
51. Oddo S, Caccamo A, Kitazawa M, Tseng BP, LaFerla FM. Amyloid deposition precedes tangle formation in a triple transgenic model of Alzheimer's disease. *Neurobiol Aging*. 2003;24:1063–1070.
52. Billings LM, Oddo S, Green KN, McGaugh JL, LaFerla FM. Intraneuronal Abeta causes the onset of early Alzheimer's disease-related cognitive deficits in transgenic mice. *Neuron*. 2005;45:675–688.
53. Gimenez-Llort L, Blazquez G, Canete T, et al. Modeling behavioral and neuronal symptoms of Alzheimer's disease in mice: a role for intraneuronal amyloid. *Neurosci Biobehav Rev*. 2007;31:125–147.
54. Neves AC, Chiquita S, Carecho R, et al. Alzheimer's disease: can the retina be a window to the brain? *Acta Ophthalmol*. 2017;95(S259).

55. Chiasseu M, Alarcon-Martinez L, Belforte N, et al. Tau accumulation in the retina promotes early neuronal dysfunction and precedes brain pathology in a mouse model of Alzheimer's disease. *Mol Neurodegener*. 2017;12:58.
56. Cordeiro MF, Guo L, Coxon KM, et al. Imaging multiple phases of neurodegeneration: a novel approach to assessing cell death in vivo. *Cell Death Dis*. 2010;1:e3.
57. Mehalow AK, Kameya S, Smith RS, et al. CRB1 is essential for external limiting membrane integrity and photoreceptor morphogenesis in the mammalian retina. *Hum Mol Genet*. 2003;12:2179–2189.
58. Kristofikova Z, Ricny J, Sirova J, Ripova D, Lubitz I, Schnaider-Beeri M. Differences between Tg2576 and wild type mice in the NMDA receptor–nitric oxide pathway after prolonged application of a diet high in advanced glycation end products. *Neurochem Res*. 2015;40:1709–1718.
59. Nam AS, Chico-Calero I, Vakoc BJ. Complex differential variance algorithm for optical coherence tomography angiography. *Biomed Opt Express*. 2014;5:3822–3832.
60. Katta N, Estrada AD, McElroy AB, et al. Laser brain cancer surgery in a xenograft model guided by optical coherence tomography. *Theranostics*. 2019;9:3555–3564.
61. Frangi AF, Niessen WJ, Vincken KL, Viergever MA. Multiscale vessel enhancement filtering. In: Wells WM, Colchester A, Delp S, eds. *Medical Image Computing and Computer-Assisted Intervention – MICCAI'98*. Berlin: Springer-Verlag; 1998:130–137.
62. Joseph A, Guevara-Torres A, Schallek J. Imaging single-cell blood flow in the smallest to largest vessels in the living retina. *Elife*. 2019;8:e45077.
63. Bradley D, Roth G. Adaptive thresholding using the integral image. *J Graphics Tools*. 2007;12:13–21.
64. Samuel MA, Zhang Y, Meister M, Sanes JR. Age-related alterations in neurons of the mouse retina. *J Neurosci*. 2011;31:16033–16044.
65. Liu B, Rasool S, Yang Z, et al. Amyloid-peptide vaccinations reduce β-amyloid plaques but exacerbate vascular deposition and inflammation in the retina of Alzheimer's transgenic mice. *Am J Pathol*. 2009;175:2099–2110.
66. Conrady AE. *Applied Optics and Optical Design, Part Two*. New York: Dover Publications; 1960.
67. Remtulla S, Hallett PE. A schematic eye for the mouse, and comparisons with the rat. *Vision Res*. 1985;25:21–31.
68. Budenz DL, Anderson DR, Varma R, et al. Determinants of normal retinal nerve fiber layer thickness measured by stratus OCT. *Ophthalmology*. 2007;114:1046–1052.
69. Peng PH, Hsu SY, Wang WS, Ko ML. Age and axial length on peripapillary retinal nerve fiber layer thickness measured by optical coherence tomography in nonglaucomatous Taiwanese participants. *PLoS One*. 2017;12:e0179320.
70. Bendschneider D, Tornow RP, Horn FK, et al. Retinal nerve fiber layer thickness in normals measured by spectral domain OCT. *J Glaucoma*. 2010;19:475–482.
71. Parikh RS, Parikh SR, Sekhar GC, Prabakaran S, Babu JG, Thomas R. Normal age-related decay of retinal nerve fiber layer thickness. *Ophthalmology*. 2007;114:921–926.
72. Feuer WJ, Budenz DL, Anderson DR, et al. Topographic differences in the age-related changes in the retinal nerve fiber layer of normal eyes measured by Stratus optical coherence tomography. *J Glaucoma*. 2011;20:133–138.
73. Harper DJ, Augustin M, Lichtenegger A, et al. Retinal analysis of a mouse model of Alzheimer's disease with multicontrast optical coherence tomography. *Neurophotonics*. 2020;7:015006.